

P-CYGNI PROFILES OF MOLECULAR LINES TOWARD ARP 220 NUCLEI

KAZUSHI SAKAMOTO¹, SUSANNE AALTO², DAVID J. WILNER³, JOHN H. BLACK², JOHN E. CONWAY²,
FRANCESCO COSTAGLIOLA², ALISON B. PECK⁴, MARCO SPAANS⁵, JUNZHI WANG⁶,
AND MARTINA C. WIEDNER⁷

Accepted for publication in The Astrophysical Journal Letters

ABSTRACT

We report ~ 100 pc ($0''.3$) resolution observations of (sub)millimeter HCO^+ and CO lines in the ultraluminous infrared galaxy Arp 220. The lines peak at two merger nuclei, with HCO^+ being more spatially concentrated than CO. Asymmetric line profiles with blueshifted absorption and redshifted emission are discovered in $\text{HCO}^+(3-2)$ and $(4-3)$ toward the two nuclei and in $\text{CO}(3-2)$ toward one nucleus. We suggest that these P-Cygni profiles are due to ~ 100 km s⁻¹ outward motion of molecular gas from the nuclei. This gas is most likely outflowing from the inner regions of the two nuclear disks rotating around individual nuclei, clearing the shroud around the luminosity sources there.

Subject headings: galaxies: active — galaxies: evolution — galaxies: individual (Arp 220)

1. INTRODUCTION

The two merger nuclei of Arp 220, about 300 pc apart on the sky (see Scoville et al. 1998, $1''=361$ pc), generate at least 40% of the total luminosity of the ultraluminous infrared galaxy ($L_{8-1000\mu\text{m}} = 10^{12.2} L_{\odot}$; Soifer et al. 1999). Each has a rotating gas disk of about 100 pc extent, the rotation axes of which are misaligned with one another (Sakamoto et al. 1999). The central 50–80 pc of the brighter western nucleus has a bolometric luminosity of $\geq 2 \times 10^{11} L_{\odot}$ according to sub-arcsec imaging of submillimeter continuum (Sakamoto et al. 2008, hereafter S08). There is also a kpc-scale molecular disk surrounding the two nuclei (Scoville et al. 1997). IR absorption analyses (e.g., Dudley & Wynn-Williams 1997; Haas et al. 2001) suggest the dominant luminosity source of Arp 220 to be compact and deeply buried, as expected in the two nuclear disks, rather than widely spread, as expected in the outer disk. Both nuclear disks host starbursts with dozens of radio supernova remnants (Parra et al. 2007) and may also contain a buried quasar (Soifer et al. 1984; Downes & Eckart 2007 and references therein; S08).

Properties of the nuclear disks, including their structure, kinematics, and gas conditions, must be elucidated in order to understand fully the nature and evolution of activity in Arp 220. In this *Letter* we report our high-resolution observations of Arp 220 in (sub)millimeter molecular lines, including its first subarcsecond resolution imaging in HCO^+ and the first detection of P-Cygni

line profiles toward the two nuclei.

2. SUBMILLIMETER ARRAY OBSERVATIONS

We observed $\text{CO}(3-2)$ and $\text{HCO}^+(4-3)$ simultaneously in 2007 May and $\text{HCO}^+(3-2)$ in 2008 August using the most extended configuration of the Submillimeter Array (SMA; Ho et al. 2004)⁸. We also used the most compact configuration in 2009 January to measure the total $\text{HCO}^+(3-2)$ flux. System gain was calibrated using two nearby quasars, J1635+381 and J1613+342. The passband over our 2 GHz-wide sidebands was calibrated using other brighter quasars. The data were reduced mostly the same way as in S08. Continuum in each sideband was collected from the channels outside of radial velocities between 4800 and 5900 km s⁻¹ in $\text{CO}(3-2)$, $\text{HCO}^+(4-3)$ and $(3-2)$, and $\text{HCN}(4-3)$ lines. The continuum was then subtracted in visibilities from line data. Phase self-calibration was made using the continuum of Arp 220. Line data were binned to 30 km s⁻¹ resolution and have velocities in the radio convention with respect to the LSR. Our spatial resolution is about $0''.3$ or 100 pc and our $\text{CO}(3-2)$ data are twice as sensitive as those in S08. Since $\text{CO}(3-2)$ was placed at the band center, our velocity coverage for $\text{HCO}^+(4-3)$ in the image band is limited to 5180 – 6840 km s⁻¹.

3. RESULTS

3.1. Compact HCO^+ and Extended CO

We detected HCO^+ , CO, and $\lambda \sim 1$ mm continuum emission associated with the two nuclei (Fig. 1). The western nucleus is more luminous than the eastern, by a factor of 2–3 in HCO^+ and continuum. The concentration of HCO^+ emission to the two nuclei is real because we detected most of the total line flux in Arp 220 (Table 1). This is in contrast to $\text{CO}(3-2)$ where only 23% of the single-dish flux was recovered even though $\text{CO}(3-2)$ and $\text{HCO}^+(4-3)$ had almost the same u-v coverage. $\text{CO}(3-2)$ emission is indeed extended on scales greater than $2''$ in

⁸ The Submillimeter Array is a joint project between the Smithsonian Astrophysical Observatory and the Academia Sinica Institute of Astronomy and Astrophysics, and is funded by the Smithsonian Institution and the Academia Sinica.

¹ Academia Sinica, Institute of Astronomy and Astrophysics, P.O. Box 23-141, Taipei 10617, Taiwan;

² Department of Radio and Space Science, Chalmers University of Technology, Onsala Space Observatory, SE 439 92 Onsala, Sweden

³ Harvard-Smithsonian Center for Astrophysics, 60 Garden St., Cambridge, MA 02138, USA

⁴ Joint ALMA Observatory, Av. El Golf 40 - Piso 18, Las Condes, Santiago 7550108, Chile

⁵ Kapteyn Astronomical Institute, P.O. Box 800, 9700 AV Groningen, The Netherlands

⁶ Department of Astronomy, Nanjing University, 22 Hankou Road, Nanjing, 210093, China

⁷ Observatoire de Paris, 61, Ave. de l'Observatoire, 75014 Paris, France

S08. Thus $\text{HCO}^+(4-3)$ and $(3-2)$ emission of Arp 220 is mostly from the two nuclear disks while the majority of $\text{CO}(3-2)$ comes from the outer disk around them. Moreover, in each nuclear disk, the HCO^+ emitting region is more compact than the CO emitting region judging from their half-peak sizes in Fig. 1.

The peak brightness temperatures (T_b) of the lines at or around each nucleus, listed in Table 1, indicate warm molecular gas in the nuclear disks. The CO peaks are about 50 K and HCO^+ about 20 K. These high T_b and high HCO^+ -to- CO intensity ratios in the nuclear disks imply that molecular gas exists there in conditions favorable for the transitions of high critical density.

3.2. *P-Cygni Line Profiles at Both Nuclei*

The line spectra at the two nuclei, in Fig. 2, show both emission and absorption. In particular, all the observed lines except $\text{CO}(3-2)$ toward the western nucleus show blueshifted absorption and redshifted emission, i.e., P-Cygni profiles. This feature is absent in our calibrator spectra.

The western nucleus has a narrow, deep absorption feature at 5340 km s^{-1} and emission at higher and lower velocities in our CO data. This profile is consistent with the previous $\text{CO}(2-1)$ profile in Downes & Eckart (2007) except that the absorption is deeper in our $\text{CO}(3-2)$ data. The deep absorption is almost at the systemic velocity of the nucleus, marked with a dashed line in Fig. 2, as expected if the CO -absorbing gas is in circular rotation in the western nuclear disk. The systemic velocity, $V_{\text{sys}}(\text{W}) = 5355 \pm 15 \text{ km s}^{-1}$, was estimated from the central velocity of the CO profile in the low-resolution ($0''.5$) data of S08, measured at half-maximum. The $\text{HCO}^+(4-3)$ and $(3-2)$ lines are also in absorption at the systemic velocity. In addition, both HCO^+ lines have absorption at blueshifted velocities while most of their emission appears at redshifted velocities. The $\text{HCO}^+(3-2)$ profile shows multiple velocity components in absorption; the minima at 4890 , 5220 , and 5340 km s^{-1} are at 3.6σ , 4.6σ , and 4.6σ , respectively. Absorption deeper than 3σ is seen down to $V_{\text{sys}}(\text{W}) - 495 \text{ km s}^{-1}$.

The eastern nucleus has very asymmetric line profiles with respect to its systemic velocity, which we estimate to be $V_{\text{sys}}(\text{E}) = 5415 \pm 15 \text{ km s}^{-1}$ in the same way as for the western nucleus. In all the observed lines, absorption is predominantly seen at or blueward of the systemic velocity while most emission is in redshifted velocities, making the profiles P Cyg type. The deepest absorption is at $45-75 \text{ km s}^{-1}$ below $V_{\text{sys}}(\text{E})$ and is 2.8σ , 4.5σ , and 3.0σ in $\text{HCO}^+(4-3)$, $(3-2)$, and $\text{CO}(3-2)$, respectively.

3.3. *Absorption Depth*

Absorption (i.e., negative intensity) in our continuum-subtracted data means absorption of the continuum, because line self-absorption alone cannot produce *negative* intensity. In order to absorb continuum the excitation temperature of the foreground gas must be below the brightness temperature of the background continuum. The (deconvolved) western nucleus has $T_b = 90-160 \text{ K}$ and a size of $50-80 \text{ pc}$ in $860 \mu\text{m}$ continuum (S08; for the SED of the two nuclei see Matsushita et al. 2009). The high T_b , due to high dust opacity in submillimeter, makes line absorption against dust continuum more likely to occur (and deeper) than at longer wavelengths.

The maximum apparent optical depth of each absorption line is in the range of $0.4-1.0$ except the $\text{HCO}^+(3-2)$ optical depth of 3.7 (or >1.4 when allowing for 1σ error) toward the eastern nucleus. The total line absorption $\int \tau_a dV$ integrated over the velocities where $\tau_a \geq 0.1$ is, in the order of $\text{HCO}^+(4-3)$, $\text{HCO}^+(3-2)$, and $\text{CO}(3-2)$, 75 , 150 , and 50 km s^{-1} toward the eastern nucleus and 85 , 82 , and 15 km s^{-1} toward the western. The absorption profiles vary among the lines, more notably toward the western nucleus. There are two caveats to keep in mind. First, our observations provide lower limits to total absorption because emission from the absorbing gas itself and from ambient (i.e., non-absorbing) gas in our beam masks the absorption. Second, our synthesized beam is larger for $\text{HCO}^+(3-2)$ than for $\text{HCO}^+(4-3)$ and $\text{CO}(3-2)$.

The absorbing column density N_{H_2} is on the order of 10^{22} cm^{-2} for the CO absorption and 10^{23} cm^{-2} for the HCO^+ if the absorbing gas is in 50 K LTE and abundances are $[\text{CO}/\text{H}_2] \approx 10^{-4}$ and $[\text{HCO}^+/\text{H}_2] \approx 10^{-8}$. The high abundance adopted for HCO^+ is consistent with recent PDR and XDR models (Meijerink & Spaans 2005), as well as models of HCO^+ enhancement in protostellar outflow shocks (Rawlings et al. 2004). The absorbing gas will have a depth on the order of $1-10 \text{ pc}$ if its density is at the $\text{CO}(3-2)$ critical density of 10^4 cm^{-3} . The actual absorbing material can be distributed over a longer length if it is inhomogeneous as in numerical hydrodynamical simulations of multi-phase gas obscuring active nuclei (e.g., Wada & Norman 2002). The column densities of the absorbing gas calculated here have large uncertainties because the absorption data provide lower limits, gas excitation conditions are poorly known, and molecular abundances can significantly vary. Still, it is possible for the absorbing column density to take these values because they are smaller than the total column density of the nuclei ($\sim 10^{25} \text{ cm}^{-2}$; S08). The remarkable detection of vibrationally excited HCN in absorption in Arp 220 (Salter et al. 2008) suggests that the excitation of HCO^+ may also be more unusual than described by our simple analysis. More realistic models of the excitation and radiative transfer of both molecules, including radiative coupling to the intense infrared continuum, will be explored in a future publication.

3.4. *Gas Motion — Rotation and Outflow*

Rotation of gas around each nucleus is evident in the $\text{CO}(3-2)$ position-velocity diagrams (Fig. 3) as the negative to positive shift of $V - V_{\text{sys}}$ across the nucleus. The CO emission ranges from 5000 to 5900 km s^{-1} around the western nucleus. The high-velocity gas around $5800-5900 \text{ km s}^{-1}$ is detected at $>3\sigma$ for the first time. The fall-off of the rotation velocity away from the nucleus agrees with the $\text{CO}(2-1)$ observations by Downes & Eckart (2007) and suggests truncation of the mass distribution of the nucleus beyond a $\lesssim 100 \text{ pc}$ core.

Radial motion of gas, in addition to the rotation, is suggested by the blueshifted absorption mentioned above. The absorbing gas must be in front of the continuum core of each nucleus and moving away from it toward us. Although absorption only tells us the gas motion along our lines of sight to the continuum nuclei, the detection of

similar blueshifted absorption on both nuclei whose nuclear disks are misaligned suggests that the gas motion is more likely a radial outflow in most directions than non-circular motion only along our sight lines. The redshifted emission in the P-Cygni profiles must then contain emission from gas on the far side of the continuum nuclei and moving away from the nuclei and us. The other emission in the spectra must be from the gas rotating in the nuclear disks.

The typical outflow velocity of the absorbing gas is probably about 100 km s^{-1} because the deepest absorption in the P-Cygni spectra is between $(V_{\text{sys}} - 45)$ and $(V_{\text{sys}} - 135) \text{ km s}^{-1}$. High-velocity components up to $\sim 500 \text{ km s}^{-1}$ are suggested toward the western nucleus by the $\text{HCO}^+(3-2)$ absorption with large velocity offsets. The absorbing gas is turbulent or has a velocity gradient across each continuum nucleus because absorption is also seen at slightly positive velocities with respect to systemic. The mass of the outflowing gas and the mass outflow rate would be on the order of $5 \times 10^7 M_{\odot}$ and $100 M_{\odot} \text{ yr}^{-1}$ if the outflowing gas with a column density of $10^{23} \text{ H}_2 \text{ cm}^{-2}$ is mostly within a radius of 50 pc (see §4.1) and has an isotropic outward velocity of 100 km s^{-1} . Note however that these numbers strongly depend on the geometry of the gas flow.

4. DISCUSSION

4.1. Location of the Absorber

The blueshifted absorbing gas is probably located in the two nuclear disks. This is likely because HCO^+ emission is concentrated to the two nuclear disks. The nuclear disks thus have significant column densities of HCO^+ excited to the $J=3$ and 4 levels, whether the excitation is collisional (with critical densities of $10^6\text{--}10^7 \text{ cm}^{-3}$ at 50 K) or by radiation. The $J=3$ HCO^+ in front of a bright source causes $\text{HCO}^+(4\leftarrow 3)$ absorption. Since column densities of excited HCO^+ must be less outside the nuclear disks according to our observations, any external gas is unlikely to be the dominant absorber.

In our preferred model, each nuclear gas disk has an inner region with significant outflow motion and an outer region dominated by rotation. This configuration can partly explain why the P-Cygni profiles are more prominent in HCO^+ than in CO. Excited HCO^+ is more concentrated toward the outflowing disk centers, while for extended CO more emission from the rotating (i.e., non-outflowing) disk likely masks absorption by the outflowing gas. It is also likely that the lower excitation temperature of HCO^+ expected from its larger Einstein A coefficients makes it a better absorber than the CO at the same location with a higher excitation temperature. The rotation-dominated part of the nuclear disk is likely the site of possible weak HNC maser that Aalto et al. (2009) suggested for the western nucleus on the basis of a narrow and bright spectral feature at the systemic velocity.

A less likely location of the absorbing gas is a few 100 pc or more from the two nuclear disks. The gas may be a part of the merger's large-scale ($> 10 \text{ kpc}$) superwind perpendicular to the kpc-scale outer molecular disk (Heckman et al. 1987; McDowell et al. 2003). The 5340 km s^{-1} absorption toward both nuclei could be explained by this common envelope model. However, the total mass

of such a gas structure would be quite large; $\sim 10^9 M_{\odot}$ for an expanding envelope of 500 pc radius and a column density of $N_{\text{H}_2} \sim 10^{22.5} \text{ cm}^{-2}$. Such an expanding molecular envelope has not been detected in emission.

4.2. Relation to Previous Observations

Observational signs of outflows from individual nuclei in Arp 220 have been scarce despite ample observations of the merger's superwind at larger scales. A biconical distribution of OH maser around the western nucleus along its rotation axis (i.e., N-S direction) was observed by Rovilos et al. (2003, their Fig. 4). Aalto et al. (2009) suggested that this emission as well as the faint HNC emission they found to be extended in the same direction may be due to an outflow from the nucleus. While kinematical evidence for the outflow is absent or inconclusive in these subarcsecond resolution observations, Baan et al. (1989) detected highly blueshifted OH maser emission with a $\sim 2'$ beam and attributed it to an outflow at 10–100 pc from the luminosity source with wind acceleration modeling. In H I observations by Mundell et al. (2001), velocities of the main absorption toward the nuclei are $V(\text{E, main H I}) = 5396 \text{ km s}^{-1}$ and $V(\text{W, main H I}) = 5325 \text{ km s}^{-1}$ after conversion from optical-heliocentric to radio-LSR. They are marginally blueshifted, by 19 and 30 km s^{-1} , from our CO-based systemic velocities. Also, the H I absorption toward the western nucleus has a subcomponent at about -80 km s^{-1} from the main component. These may be related to the molecular outflows that we suggest.

4.3. Nuclear Winds and the Nuclear Disks

The P-Cygni profiles toward the two nuclei provide a new clue to the energetic nucleus of Arp 220. The nuclear disks need to be reinvestigated in light of the suggested nuclear winds.

The compact and luminous sources in the nuclei probably make the outflows inevitable. For example, supernovae inject $3 \times 10^{50} \text{ J}$ of mechanical energy into the western nucleus in 1 Myr for the supernova rate of $\sim 3 \text{ yr}^{-1}$ that Lonsdale et al. (2006) observed. (The rate is $\sim 1 \text{ yr}^{-1}$ for the eastern nucleus.) If 10% of this is passed to kinetic energy of $10^8 M_{\odot}$ of gas, the gas velocity will be 500 km s^{-1} . Gas at shallow parts of the gravitational potential or getting more energy than average will escape the nucleus. Although the outflow may be mostly ionized, it will entrain molecular gas on its way. Radiation pressure on dust also drives an outflow in the case of a very compact starburst or an AGN buried in dust (Scoville et al. 2001; Scoville 2003; Murray et al. 2005). The momentum of a $5 \times 10^7 M_{\odot}$ gas outflowing at 100 km s^{-1} is equivalent to the total momentum of photons that a $0.5 \times 10^{12} L_{\odot}$ source radiates in 0.5 Myr. Such an outflow may be more isotropic near its origin than the outflow caused by a disk starburst and would be more significant in the inner region of each nuclear disk because the radiation pressure declines with radius as r^{-2} .

The winds are important for the evolution of the nuclear disks because they remove the shroud of and fuel for the buried energy sources. The small crossing time of the nuclear winds over each disk, $\lesssim 1 \text{ Myr}$, is suggestive in terms of the evolution. It is either that we are seeing very young winds or that the gas motion in each disk is

not purely outward in every direction despite the large opening angles of the outflows inferred in §3.4. For the latter, it is conceivable that high-density gas in the mid-plane of each nuclear disk is little affected by the outflow and even has inward motion due to viscosity to replenish gas to the center, as in Wada & Norman (2002). The evolution of the nuclear gas disks is then determined by the balance of the gas accretion, gas outflow, and gas consumption by star formation and AGN until the coalescence of the nuclei and of the gas disks.

We are grateful to the SMA staff who made these observations possible. We thank the referee for helpful comments and K. S. thanks Dr. Keiichi Wada for stimulating discussion. This research made use of the NASA/IPAC Extragalactic Database (NED) and NASA's Astrophysics Data System (ADS).

Facilities: SMA

REFERENCES

- Aalto, S., Wilner, D., Spaans, M., Wiedner, M., Sakamoto, K., Black, J., & Caldas, M. 2009, *A&A*, 493, 481
 Baan, W. A., Haschick, A. D., & Henkel, C. 1989, *ApJ*, 346, 680
 Downes, D., & Eckart, A. 2007, *A&A*, 468, L57
 Dudley, C. C., & Wynn-Williams, C. G. 1997, *ApJ*, 488, 720
 Greve, T. R., Papadopoulos, P. P., Gao, Y., & Radford, S. J. E. 2009, *ApJ*, 692, 1432
 Haas, M., Klaas, U., Müller, S. A. H., Chini, R., & Coulson, I. 2001, *A&A*, 367, L9
 Heckman, T. M., Armus, L., & Miley, G. K. 1987, *AJ*, 93, 276
 Ho, P. T. P., Moran, J. M., & Lo, K. Y. 2004, *ApJ*, 616, L1
 Lonsdale, C. J., Diamond, P. J., Thrall, H., Smith, H. E., & Lonsdale, C. J. 2006, *ApJ*, 647, 185
 Matsushita, S. et al. 2009, *ApJ*, 693, 56
 McDowell, J. C., et al. 2003, *ApJ*, 591, 154
 Meijerink, R., & Spaans, M. 2005, *A&A*, 436, 397
 Mundell, C. G., Ferruit, P., & Pedlar, A. 2001, *ApJ*, 560, 168
 Murray, N., Quataert, E., and Thompson, T. A. 2005, *ApJ*, 618, 569
 Parra, R., Conway, J. E., Diamond, P. J., Thrall, H., Lonsdale, C. J., Lonsdale, C. J., & Smith, H. E. 2007, *ApJ*, 659, 314
 Rawlings, J. M. C., Redman, M. P., Keto, E., & Williams, D. A. 2004, *MNRAS*, 351, 1054
 Rovilos, E., Diamond, P. J., Lonsdale, C. J., Lonsdale, C. J., & Smith, H. E. 2003, *MNRAS*, 342, 373
 Sakamoto, K., Scoville, N. Z., Yun, M. S., Crosas, M., Genzel, R., & Tacconi, L. J. 1999, *ApJ*, 514, 68
 Sakamoto, K. et al. 2008, *ApJ*, 684, 957 (S08)
 Salter, C. J., Ghosh, T., Catinella, B., Lebron, M., Lerner, M. S., Minchin, R., & Momjian, E. 2008, *AJ*, 136, 389
 Scoville, N. Z., Yun, M. S., & Bryant, P. M. 1997, *ApJ*, 484, 702
 Scoville, N. Z., et al. 1998, *ApJ*, 492, L107
 Scoville, N. Z., Polletta, M., Ewald, S., Stolovy, S. R., Thompson, R., and Rieke, M. 2001, *ApJ*, 122, 3017
 Scoville, N. Z. 2003, *J. Korean Astron. Soc.*, 36, 167
 Soifer, B. T. et al. 1984, *ApJ*, 283, L1
 Soifer, B. T. et al. 1999, *ApJ*, 513, 207
 Wada, K., & Norman, C. A. 2002, *ApJ*, 566, L21
 Wiedner, M. C., Wilson, C. D., Harrison, A., Hills, R. E., Lay, O. P., & Carlstrom, J. E. 2002, *ApJ*, 581, 229

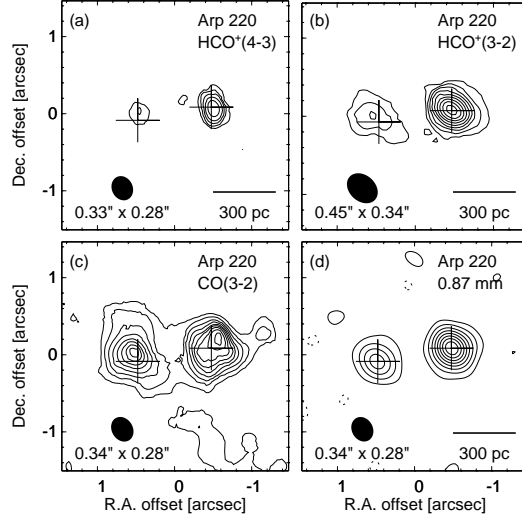


FIG. 1.— Integrated intensity maps of $\text{HCO}^+(4-3)$, $(3-2)$, and $\text{CO}(3-2)$ lines and 0.87 mm continuum. The line moment-0 maps were made using positive signals only. The lowest contour is at 2σ and the n -th contour is at $9.5n$, $4.3n$, and $10.3n \text{ Jy beam}^{-1} \text{ km s}^{-1}$ in (a), (b), and (c), respectively, and at $14.4n^{1.5} \text{ mJy beam}^{-1}$ in (d). Crosses are at continuum peaks and filled ellipses show synthesized beams.

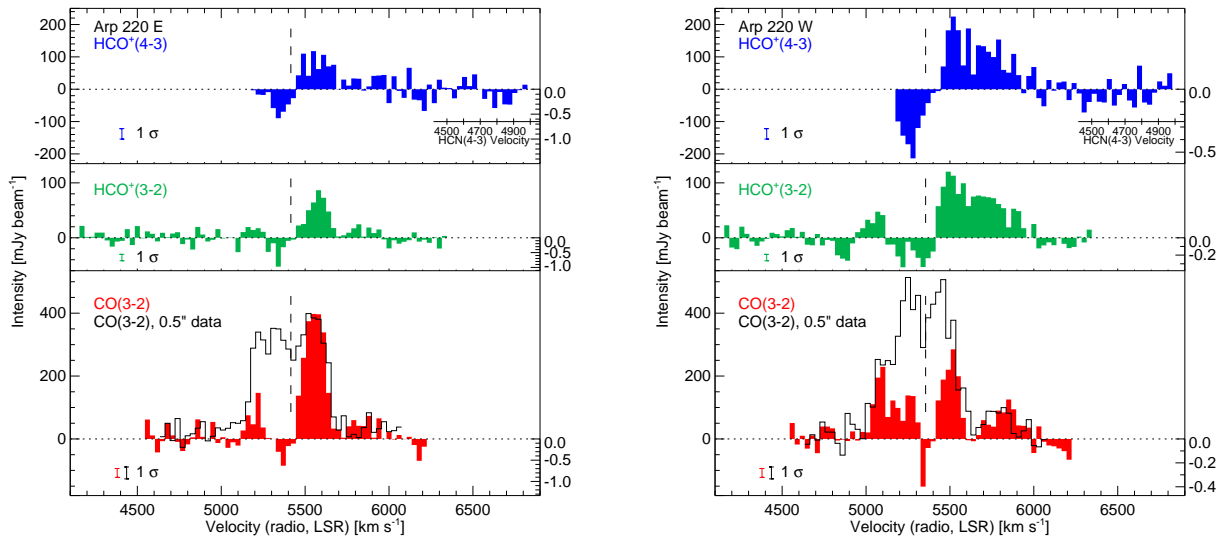


FIG. 2.— Molecular-line spectra at the two nuclei of Arp 220. Continuum has been subtracted. The right ordinate is the fractional absorption depth f_a with respect to the continuum intensity of each nucleus, and can be converted to optical depth via $\tau_a = -\log(-f_a)$. The 1σ noise is 32, 12, and 28 mJy beam^{-1} for $\text{HCO}^+(4-3)$, $(3-2)$, and $\text{CO}(3-2)$, respectively. The $\text{CO}(3-2)$ spectra overplotted in black are from $0''.5$ -resolution data in Sakamoto et al. (2008). The systemic velocity that we estimated for each nucleus is shown by a dashed line.

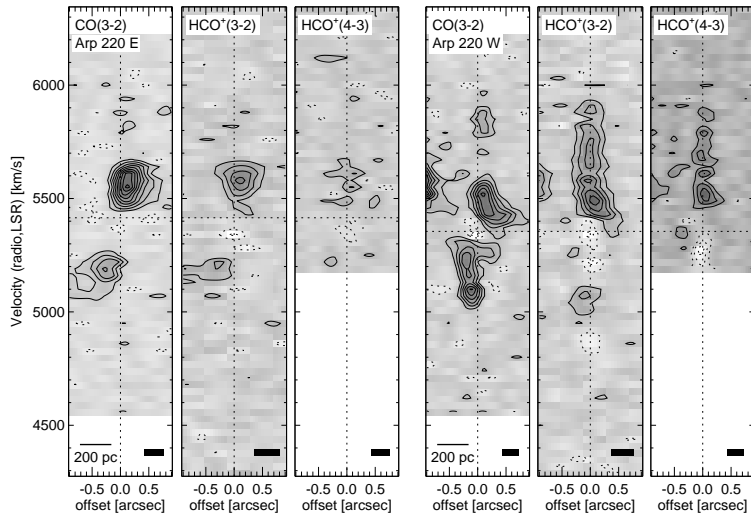


FIG. 3.— Position-velocity diagrams of Arp 220 nuclei. Position is measured from each nucleus along the position angle of 45° for the eastern nucleus and 270° for the western. Contours are at $2n\sigma$ ($n = \pm 1, \pm 2, \dots$) with negative ones dashed. The rms noise in brightness temperature is 3.1, 1.3, and 3.5 K for CO(3–2), HCO⁺(3–2), and (4–3), respectively. The horizontal dotted lines are at the systemic velocities of the nuclei, and the black rectangles show the spatial and velocity resolutions.

TABLE 1
OBSERVED PARAMETERS OF ARP 220

Parameter	East	West	All	f_{tot}^1
$S_{\text{CO}(3-2)}$ [Jy km s ⁻¹]	250	301	$(7.0 \pm 1.1) \times 10^2$	0.23 ± 0.06
$S_{\text{HCO}^+(4-3)}$ [Jy km s ⁻¹]	19	61	$(1.1 \pm 0.2) \times 10^2$	1.0 ± 0.3
$S_{\text{HCO}^+(3-2)}$ [Jy km s ⁻¹]	35	63	$(1.0 \pm 0.1) \times 10^2$	0.64 ± 0.13
$S_{0.87 \text{ mm}}$ [Jy]	0.18	0.49	0.68 ± 0.10	1.0 ± 0.2
$S_{1.1 \text{ mm}}$ [Jy]	0.07	0.20	0.27 ± 0.03	0.82 ± 0.15
CO(3–2) max T_b [K]	58 (66)	40 (47)
HCO ⁺ (4–3) max T_b [K]	16 (24)	26 (34)
HCO ⁺ (3–2) max T_b [K]	12 (17)	15 (21)
0.87 mm max T_b [K]	16 (23)	42 (50)
1.1 mm max T_b [K]	7 (12)	20 (25)
$V_{\text{sys}}(\text{radio, LSR})$ [km s ⁻¹]	5415 ± 15	5355 ± 15

NOTE. — We conservatively estimate flux-calibration 1σ errors to be 10% and 15% for 0.86 and 1.1 mm bands, respectively. Line fluxes are integrated over 4800–5900 km s⁻¹ [5200–5900 km s⁻¹ for HCO⁺(3–2)] including both emission and absorption. Peak brightness temperatures are measured at or around each nucleus without correcting for beam dilution or missing flux. The first one is Rayleigh-Jeans T_b and the second in parenthesis is Planck T_b .

¹ Fraction of the flux (or flux density) recovered in our $0''.3$ -resolution data with respect to the total flux of Arp 220. The total fluxes are 106 ± 23 Jy km s⁻¹ for HCO⁺(4–3) (Greve et al. 2009), $(3.0 \pm 0.6) \times 10^3$ Jy km s⁻¹ for CO(3–2) in the central $14''$ (Wiedner et al. 2002), 152 ± 26 Jy km s⁻¹ for HCO⁺(3–2) (This work. SMA sub-compact array observations with the minimum projected baseline of 9 m), 0.7 ± 0.1 Jy for 0.87 mm continuum (S08 and reference therein), and 0.33 ± 0.05 Jy for 1.1 mm continuum (This work, SMA sub-compact configuration).